frontiers | Frontiers in Energy Research

TYPE Original Research
PUBLISHED 17 September 2025
DOI 10.3389/fenrg.2025.1650577



OPEN ACCESS

EDITED BY
Lin Liu,
University of Technology Sydney, Australia

REVIEWED BY
Omveer Singh,
Gautam Buddha University, India
Cunhe Li,
Shandong University of Technology, China

*CORRESPONDENCE
Xiangli Deng,
xiangli_deng@163.com

RECEIVED 23 June 2025
ACCEPTED 01 September 2025
PUBLISHED 17 September 2025

CITATION
Wang J, Tong Z, Zhang K, Liu Y, Deng X and Tu H (2025) Research on transformer early fault diagnosis based on fiber - optic leakage magnetic field measurement.
*Front. Energy Res.* 13:1650577.
doi: 10.3389/fenrg.2025.1650577



# Research on transformer early fault diagnosis based on fiber - optic leakage magnetic field measurement

Junchao Wang[1], Zhixiang Tong[1], Kun Zhang[1], Yaqi Liu[1], Xiangli Deng[2]* and Hang Tu[2]

[1]China Yangtze Power Company, Kunming, China, [2]School of Electrical Engineering, Shanghai University of Electric Power, Shanghai, China

When a severe fault occurs within a transformer, the fault current escalates rapidly, making it challenging for differential protection systems to promptly isolate the faulty transformer. This delay can lead to catastrophic accidents, such as explosive combustion. To address this issue, this study proposes a novel differential protection device based on leakage magnetic field characteristics. The device accurately detects transformer winding deformation, arc-type faults, and inter-turn faults during the early stages of transformer faults, thereby preventing severe accidents. By analyzing several early transformer fault cases, this study proposes leveraging the symmetry characteristics of the leakage magnetic field to identify early faults. A fiber-optic sensor, utilizing the Faraday magneto-optical effect, is developed to measure leakage magnetic field characteristics. Based on this, a differential protection scheme incorporating steady-state and transient leakage magnetic field quantities is proposed to identify winding deformation and inter-turn faults. A prototype of the protection device has been developed, successfully passing static and dynamic simulation tests, and is slated for deployment in field operations.

KEYWORDS

**transformer protection, transformer early faults, leakage magnetic field, field test, magnetic sensing**

## 1 Introduction

Power transformers, vital components of power system equipment whose faults can disrupt electrical supply and incur significant economic losses, should maintain operational reliability to ensure the safety and stability of the power system (Yan et al., 2024). Internal faults in these transformers may activate protective mechanisms, potentially interrupting the power supply. If circuit breakers fail to trip promptly, arc discharges can cause oil decomposition, generating elevated temperatures and pressures that may lead to catastrophic accidents, such as explosive combustion. Such incidents can lead to substantial economic losses for both the state and power utilities (Brodeur and Dastous, 2020). Consequently, investigating the mechanisms of incipient transformer faults and developing early fault detection devices are essential. These devices facilitate prompt identification of internal faults, evaluation of their progression, and execution of appropriate protective measures, thereby minimizing maintenance costs and enhancing power supply reliability.

Prior to commissioning, power transformers may experience mechanical shocks during transportation and installation. During operation, they may be subjected to elevated short-circuit currents caused by external faults. Combined with insulation aging, these factors can cause irreversible winding deformation, inter-turn arc faults, or inter-turn short circuits (Wang et al., 2016; Xian et al., 2024), potentially leading to catastrophic accidents such as transformer explosions (Abi-Samra et al., 2009). Current engineering practices primarily rely on differential protection and gas relay protection (Mirowski and LeCun, 2012; Gomathi et al., 2023). However, minor insulation damage within the windings often produces current changes too small to reliably trigger differential protection. Protection typically activates only after the fault escalates beyond the threshold, by which point severe winding damage may have already occurred. Notably, even minor insulation faults alter the leakage magnetic field distribution around the windings. Leveraging this magnetic variation as a diagnostic feature can significantly enhance fault detection sensitivity.

Recent studies have advanced fault diagnosis by leveraging variations in leakage magnetic fields. For instance, Reference (Ji et al., 2024) conducted finite element simulations of various winding deformations, proposing a defect encoding method based on magnetic field changes with practical applications. Zhou and Wang (2017) explored the correlation between winding deformation and leakage magnetic field distribution, developing a classification method based on this characteristic. Deng et al. (2023a) formulated an analytical multi-state model aligned with actual transformer behavior, utilizing differences in leakage magnetic fields to detect and locate early winding faults. Zheng et al. (2022) derived the spatial magnetic flux density distribution of windings, validating leakage field patterns under inter-turn faults through simulation. Zhang et al. (2021) developed a coupled electromagnetic-circuit model, conducting multi-physics analysis to characterize inter-turn faults and provide a theoretical foundation for improving transformer short-circuit withstand capabilities. Deng et al. (2023b) utilized leakage magnetic fields as features in a deep belief network to diagnose winding deformation. Liu et al. (2024a) and Liu et al. (2024b) employed finite element model data to select fault features and trained machine learning models for classification. However, these approaches often rely on simulated data and complex parameter tuning rather than analyzing the physical mechanisms of early winding faults, potentially compromising protection sensitivity and reliability. In contrast, Haghjoo et al. (2018) proposed a method for fault phase identification by examining symmetry changes in leakage field distributions before and after winding faults.

To utilize leakage magnetic field characteristics as protective triggers, highly sensitive magnetic field sensors suitable for high-voltage, high-current environments are essential. Current magnetic field sensors include magnetoresistive sensors, induction coils, and magneto-optical sensors. The former two, being metallic, present installation challenges and risks of short circuits (Yamagashira et al., 2014; Zhang et al., 2019; Li et al., 2021). In contrast, fiber-optic magneto-optical sensors, leveraging the Faraday effect, provide high resolution, robust insulation reliability, and cost-effectiveness. These sensors detect magnetic field variations through optical polarization, making them well-suited for measuring transformer leakage magnetic fields (Jiang et al., 2021; Huang et al., 2024). Consequently, early transformer faults can be identified by monitoring changes in leakage magnetic field characteristics (Deng et al., 2024).

The reviewed literature confirms the feasibility of leveraging leakage magnetic field distributions for early transformer fault detection. However, most existing approaches remain at the theoretical stage, facing challenges in measuring magnetic fields in high-voltage, high-EMI environments and conducting dynamic model tests for incipient faults. As a result, commercialized products or practical engineering applications have yet to be realized.

To address these limitations, this study analyzes real-world cases of incipient transformer faults, develops analytical and simulation models based on physical structural parameters, and examines leakage magnetic field characteristics across various fault types in high-, medium-, and low-voltage windings. A novel protection scheme, utilizing steady-state and transient leakage magnetic field differentials, is proposed. Its effectiveness has been validated through comprehensive static and dynamic tests, leading to the development of an early fault protection system for transformers, suitable for engineering applications.

## 2 Case study of early transformer failure on site

From 2015 to 2020, a 100 MVA step-up transformer in a wind farm in Shandong Province experienced four internal faults, as summarized in Table 1. Post-fault inspections revealed that the winding insulation structures were damaged, with deformations at the winding ends. Additionally, severe overheating led to charring, copper particle detachment, and inter-turn discharge faults. Although the transformer was equipped with online monitoring systems such as dissolved gas analysis and partial discharge detection, these systems failed to detect the faults. Due to the minor nature of the internal faults in their initial stages, the sensitivity of the differential protection was insufficient to trigger a response. Consequently, the faults escalated until the protection system acted, by which time the windings had been severely burnt.

On June 4 at 21:01, an internal fault occurred in a ±800 kV converter transformer. All three differential protection systems activated simultaneously, and 22 m later, the "Y-connection minor differential power-frequency component" protection was triggered. As a result, the transformer windings were severely burnt and rendered irreparable. Similarly, in a hydropower station, an inter-turn short circuit occurred within the low-voltage winding of an excitation transformer. Although the differential protection systems operated, the insulation caught fire and burned, severely damaging the transformer and disrupting normal operations.

These cases highlight several shortcomings in existing protection strategies, despite the presence of traditional online monitoring and protection systems. Online monitoring is typically effective only during the insulation degradation stage. Since partial discharges occur within the insulation, the current waveform of the windings often remains unchanged, making fault detection difficult. Therefore, the reliability of traditional online systems is relatively low. While conventional differential protection reliably activates in the event of severe faults, such events evolve rapidly and may cause irreversible damage before action is taken.

TABLE 1 Maintenance record of the 100MVA confluence main transformer in a wind farm in shandong province.

| Record No. | Operation time | Reason for repair | Fault description |
|---|---|---|---|
| 1 | 2015–2016 | Differential protection action | The two cakes at the end of the high-voltage C-phase coil are burned out |
| 2 | 2016–2018 | Excessive acetylene, differential protection action, light gas alarm | Large area discharge of C-phase coil, short circuit in the middle turn, deformation of 20 turns, carbonization and detachment of insulation on the surface of the wire |
| 3 | 2018–2019 | Oil and gas exceeding the standard | During peak power generation periods, replace the main transformer |
| 4 | 2019–2020 | No load closing heavy gas protection action, acetylene exceeds the standard | B-phase deformation, minor malfunction, high-voltage C-phase tail coil burnt out |

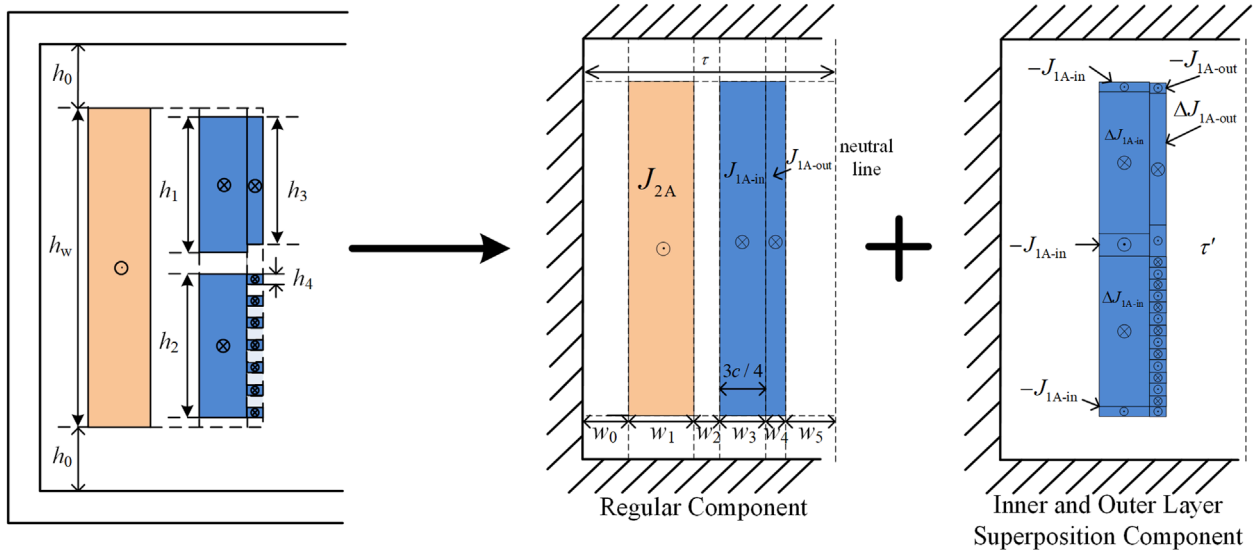


FIGURE 1
Calculation model for leakage magnetic field of transformer winding.

Between the stages of insulation degradation and severe fault lies a critical early-stage fault period. Although current waveforms exhibit only subtle variations during this stage, the leakage magnetic field distribution around the faulted windings changes significantly. By exploiting these changes in the leakage magnetic field, early-stage winding faults can be reliably detected in time to de-energize the transformer, reducing maintenance costs and improving overall grid security.

# 3 Analytical calculation and simulation of transformer leakage magnetic field

## 3.1 Analytical calculation of transformer leakage magnetic field

To investigate the leakage magnetic field distribution under normal operating conditions and inter-turn short-circuit faults, an analytical model of the transformer winding is first established. For medium and small capacity transformers, due to insulation design considerations, the heights of the high- and low-voltage windings are typically not identical, and a gap is generally present in the middle section. To ensure consistency between theoretical analysis and dynamic simulation experiments, the model is based on an actual laboratory dry-type transformer. As shown in Figure 1, the calculated region ignores the shielding effects of the yoke and assumes equal ampere-turns for the high- and low-voltage windings, assuming the magnetic permeability of the iron core $\mu_{Fe} = \infty$.

To handle the irregular winding geometry, the model is decomposed into a symmetrical regular part and an irregular superimposed section representing the high-voltage winding. This decomposition is illustrated in Figure 1. The leakage magnetic field distribution of each section is calculated separately and then superimposed to obtain the overall field distribution.

The leakage magnetic field in each region is solved using the method of separation of variables under specified boundary

TABLE 2 Main nameplates and dimensional parameters of transformers.

| Parameter | Numerical value | Parameter | Numerical value |
|---|---|---|---|
| Rated capacity/kVA | 50 | Rated voltage/kV | 1/0.4 |
| Rated current/A | 28.87/72.17 | Rated frequency/Hz | 50 |
| No load current (%) | 3.44 | No load loss/W | 257.4 |
| Low voltage winding height/mm | 350 | Height of each section of high-voltage non tightly wound winding/mm | 19 |
| Low voltage winding thickness/mm | 15 | High voltage winding thickness/mm | 22.5 |
| Height of lower section of inner high-voltage winding/mm | 174 | Height of upper section of outer high-voltage winding/mm | 102 |
| Height of upper section of inner high-voltage winding/mm | 116 | Distance between upper and lower sections of outer high-voltage winding/mm | 34 |
| Low voltage winding turns | 139 | High voltage winding turns | 201 |

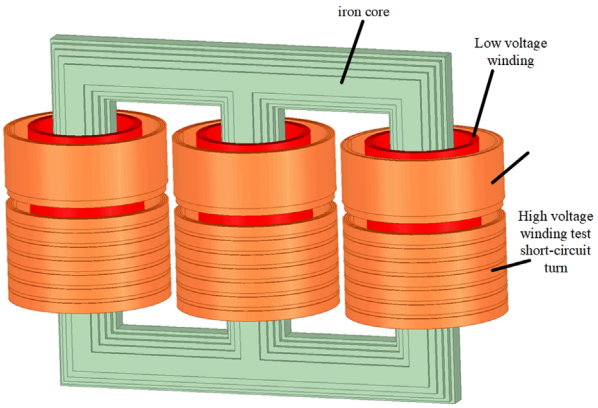


FIGURE 2
Simulation model of three-phase segmented irregular winding transformer.

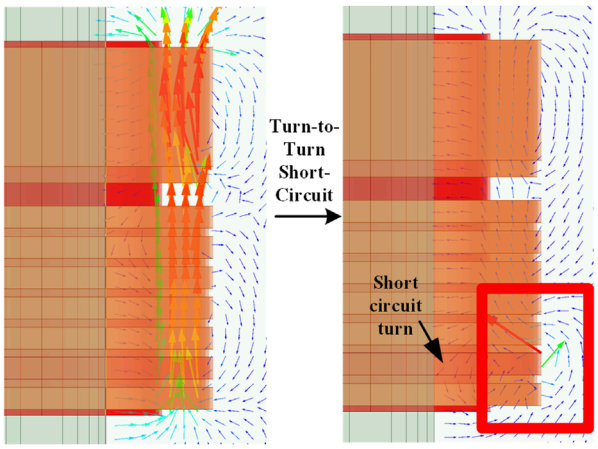


FIGURE 3
Distribution of transformer magnetic vectors under normal operating condition vs. inter-turn short circuit.

conditions by applying the Laplace and Poisson equations. By using the mirror method to $x(0 \sim \tau)$ extend the current density in this region, it can be transformed into a periodic function and expanded into a continuous Fourier series. The calculation region is divided into Regions I, II, and III. At the interfaces between regions, the axial components of the magnetic vector potential and the magnetic field intensity are continuous. At the interface with the magnetic core, the axial component is zero. The governing equations for each region are as shown in Equation 1.

$$\begin{cases} \dfrac{\partial^2 A_{zI}}{\partial x^2} + \dfrac{\partial^2 A_{zI}}{\partial y^2} = -\mu_0 J_z \\ \dfrac{\partial^2 A_{zII}}{\partial x^2} + \dfrac{\partial^2 A_{zII}}{\partial y^2} = 0 \\ \dfrac{\partial^2 A_{zIII}}{\partial x^2} + \dfrac{\partial^2 A_{zIII}}{\partial y^2} = 0 \end{cases} \tag{1}$$

Solving these equations and summing the components yields the magnetic vector potentials $A_z$ for Regions I, II, and III. By taking derivatives, the magnetic flux densities in various directions are obtained. In particular, the transverse magnetic flux density in each region, derived by differentiating with respect to the vertical coordinate, is expressed in Equation 2.

$$\begin{cases} B_{xI} = \dfrac{\mu_0 \tau J_{mA}}{2m\pi} \sum\limits_{m=1}^{\infty} \left[ -e^{m\frac{\pi}{\tau}(y-(h_w+h_0))} + e^{m\frac{\pi}{\tau}(h_0-y)} \right] \cos m\dfrac{\pi}{\tau}x \\ B_{xII} = -\dfrac{\mu_0 \tau J_{mA}}{2m\pi} \sum\limits_{m=1}^{\infty} \left[ e^{m\frac{\pi}{\tau}(h_w+h_0)} - e^{m\frac{\pi}{\tau}h_0} \right] e^{-m\frac{\pi}{\tau}y} \cos m\dfrac{\pi}{\tau}x \\ B_{xIII} = \dfrac{\mu_0 \tau J_{mA}}{2m\pi} \sum\limits_{m=1}^{\infty} \left[ e^{-m\frac{\pi}{\tau}h_0} - e^{-m\frac{\pi}{\tau}(h_w+h_0)} \right] e^{m\frac{\pi}{\tau}y} \cos m\dfrac{\pi}{\tau}x \end{cases} \tag{2}$$

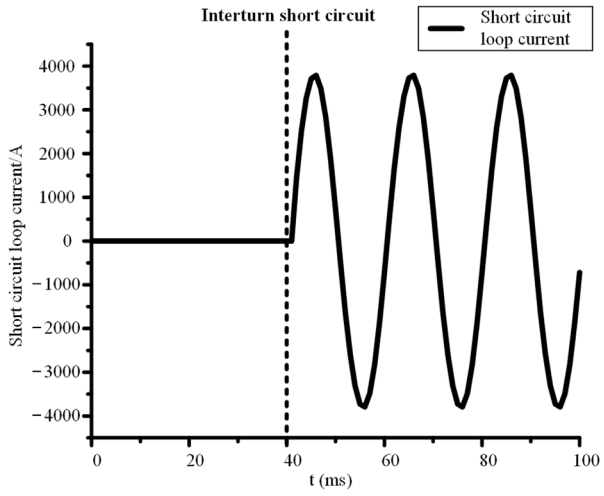


FIGURE 4
Simulation waveform of short-circuit loop current.

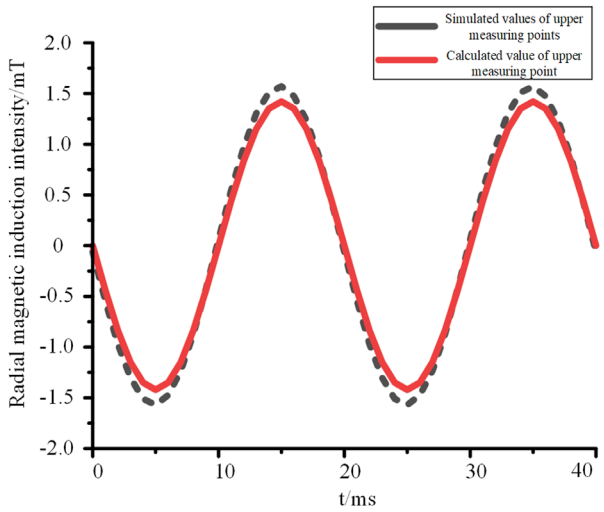


FIGURE 5
Comparison between analytical calculation and simulation of transformer leakage magnetic field.

## 3.2 Simulation analysis of transformer leakage magnetic field

Due to the limitations of short-circuit current capacity in physical dynamic simulation experiments, scenarios involving large short-circuit currents cannot be tested directly. Additionally, specific requirements of algorithm verification necessitate the development of a finite element simulation model corresponding to the physical transformer, such as modeling short circuits at any turn. Based on the nameplate data and structural parameters of the early fault test transformer listed in Table 2, a three-dimensional finite element model was constructed using ANSYS Maxwell, as illustrated in Figure 2. The laminated structure of the transformer core was simplified, and the low-voltage winding was modeled as a single concentric cylinder. The high-voltage winding assembly was divided into upper and lower sections according to its actual configuration, with a gap in the middle. The upper section was simplified as a complete concentric cylinder, while the lower section contained seven taps used to connect external circuits. These taps allowed for the simulation of minor inter-turn short-circuit faults by connecting fixed resistors. The faulted winding section was simplified into seven identical concentric cylindrical segments. The external circuit was co-simulated using the Simplorer simulator to analyze the behavior of the system under slight inter-turn short-circuit conditions.

Taking an inter-turn short-circuit fault occurring at the lower section of phase A's high-voltage winding at t = 40 ms as an example, the coupled simulation between Maxwell's magnetic solver and Simplorer's circuit solver was conducted. The leakage magnetic field distribution before and after the fault, the radial magnetic flux density at different measurement points, the current in the short-circuit loop, and the terminal current were analyzed. These results were compared with those from the analytical model to identify fault characteristics and develop protection criteria.

Under normal conditions, the 3D distribution of magnetic flux density vectors shows that the magnetic vectors at the winding ends bend and diverge, dominated by radial components. Along the axial direction outside the winding, the magnetic flux density is at its maximum and exhibits symmetry between the upper and lower parts, as shown in Figure 3.

Following the occurrence of a minor inter-turn short-circuit fault, Figure 2 shows that significant changes occur in the magnetic vector distribution around the fault region. This is because, after the short circuit occurs at t = 40 ms, the current in the fault loop rises to 3793 A, as shown in Figure 4, which is several tens of times higher than under normal operating conditions. Such high localized current drastically alters the surrounding leakage magnetic field, forming a pronounced vortex-shaped closed magnetic loop around the faulted turns. These magnetic vectors exhibit a concentric circular pattern, and the reverse magnetic field generated by the short-circuit current destroys the symmetry of the original leakage magnetic field distribution.

To validate the consistency between the simulation model and the analytical calculations, the radial magnetic flux density curves at the upper winding measurement points under the same load current conditions were plotted. As shown in Figure 5, the results of both methods are in close agreement.

From the above simulations, it is evident that inter-turn faults disrupt the symmetry of the leakage magnetic field distribution. The consistency between the analytical and simulation results confirms the accuracy of the analytical model. However, the 3D FEM more closely represents the actual transformer structure and offers higher precision in capturing field distortions, including the influence of the core. Therefore, for future simulations of inter-turn faults, the FEM model will be used, while the analytical model will support protection threshold calculations.

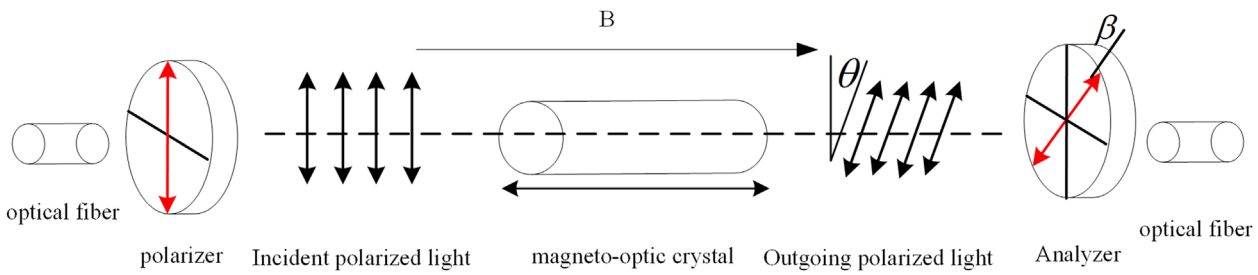


FIGURE 6
Principle of Faraday magneto-optical effect.

# 4 Principle of leakage magnetic field measurement and differential protection

## 4.1 Principle of magnetic field measurement using fiber optic sensors

The basic principle of magnetic field measurement using fiber optic sensors is based on the Faraday magneto-optical effect. As illustrated in Figure 6, light emitted from a laser source passes through a polarizer and becomes linearly polarized. When the polarized light travels through a magneto-optic crystal, the presence of a vector magnetic field along the direction of light propagation causes a rotation in the plane of polarization. This rotation angle θ is dependent on the magnetic flux density (Hou et al., 2024), as expressed in Equation 3:

$$\theta = VlB \tag{3}$$

After passing through the magneto-optic material and undergoing a rotation of θ, the incident linearly polarized light becomes the output polarized light. It then passes through an analyzer and enters the tail fiber, ultimately reaching the photoelectric conversion module. According to Malus' Law, the input voltage $U_0$ of the sampling circuit can be expressed as:

$$U_0 = KL_i e^{-\alpha l}\cos^2(\beta + VlB) = \frac{KL_i e^{-\alpha l}}{2}\left(1 - \sin\left(2VlB_m \sin(\omega t + \varphi)\right)\right) \tag{4}$$

As shown in Equation 4, the output voltage of the optical measurement module is significantly affected by light intensity and temperature. Variations in input light intensity $L_i$ can cause large fluctuations in the amplitude of the measured signal but do not affect its phase. The laser emitter and photodetector in the protection system are configured with single-port emission and reception, and the optical power of each channel remains constant. Under stable conditions without external physical disturbances, $U_0$ maintains a fixed proportional relationship with $L_i$. The Verdet constant $V$ is notably temperature-sensitive, with a temperature coefficient that can reach 0.3/°C. within the IEC standard ambient temperature range of −25 °C to 40 °C, the maximum and minimum values of the Verdet constant may differ by a factor of 1.95, affecting the amplitude of the fundamental component of $U_0$. However, in dry-type transformer applications, ambient temperature variations are slow. By applying protection logic delay differential and a temperature correction factor in software, the influence of temperature-related factors is eliminated. This enables accurate acquisition of the one-dimensional scalar leakage magnetic flux density along the axis of the magneto-optic crystal by reading and processing the voltage $U_0$.

## 4.2 Principle of leakage magnetic field differential protection

During the normal operation of a power transformer, the distribution of electromagnetic forces within the winding must be balanced, and audible noise must remain within acceptable limits. As a result, the leakage magnetic field near the windings exhibits a symmetric distribution, as shown in Figure 7A. Although factors such as tap windings and sectionalized winding structures may slightly affect the symmetry, air acts as a linear medium, and the symmetry of the leakage field distribution can be compensated by selecting appropriate sensor positions. When a minor inter-turn fault occurs, the current in the shorted turns becomes extremely large, causing significant changes in the local leakage magnetic field. This disturbs the symmetry of the field distribution, as illustrated in Figure 7B.

In the case of a minor internal inter-turn fault, the current distribution in the winding and the corresponding leakage magnetic flux lines are illustrated in Figure 7C. The leakage field generated by the fault current primarily affects the space surrounding the fault point, with minimal influence on distant regions. Therefore, the winding region can be divided into three zones, as shown in Figure 7D. Magnetic field sensors are deployed at the boundaries of these regions to facilitate the detection of leakage field variations and the localization of the fault point (Deng et al., 2022).

When an inter-turn fault occurs in a transformer, conventional differential protection schemes based on current transformers located at the transformer terminals cannot sense the fault current circulating within the shorted turns. However, the radial leakage flux generated by the fault current can be effectively detected by magnetic field sensors. Therefore, differential protection based on magnetic field measurement provides significantly higher sensitivity than traditional current differential protection.

An inter-turn short circuit alters the spatial distribution of the leakage magnetic field, resulting in a sudden increase in

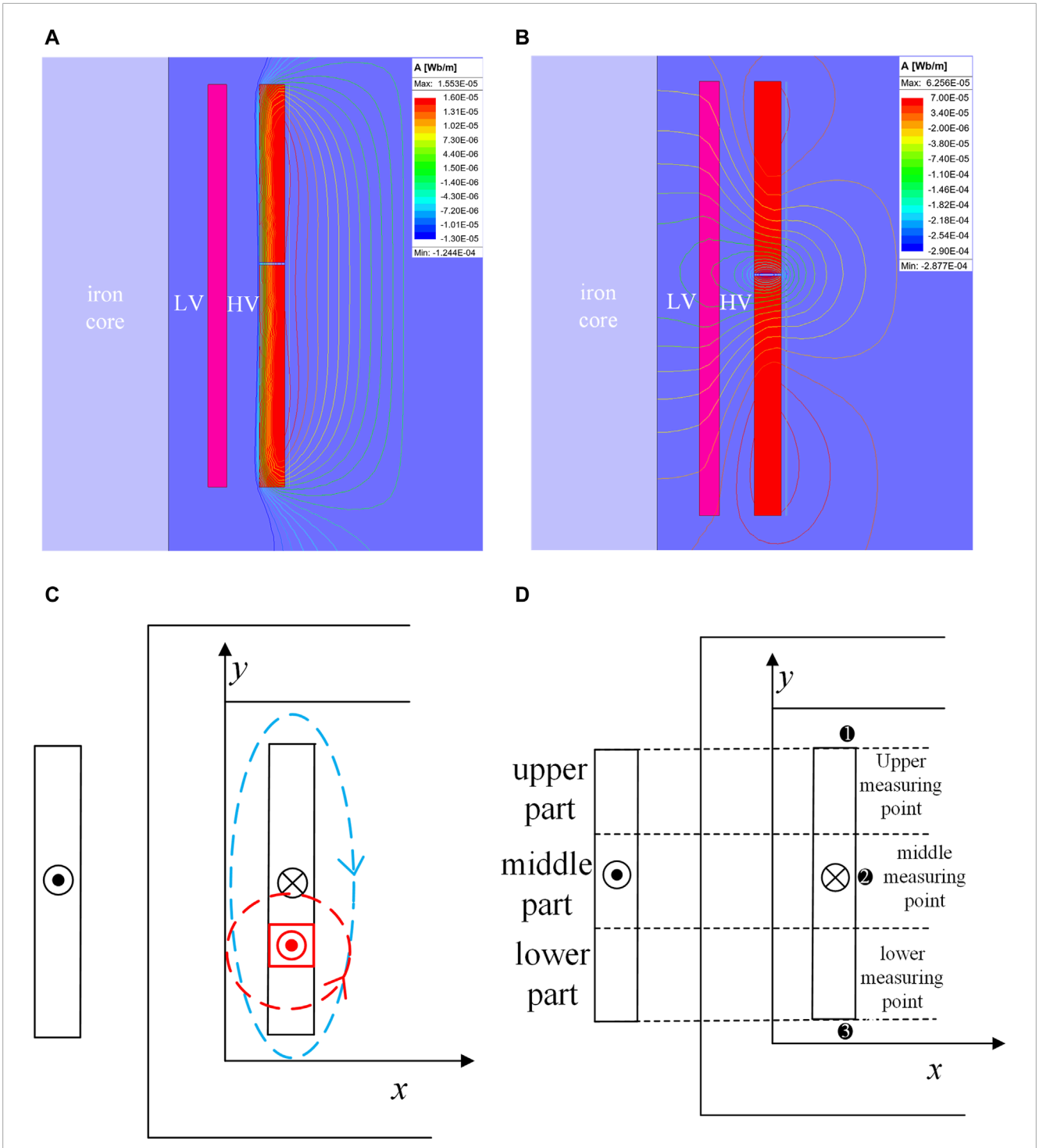


FIGURE 7
Transformer leakage magnetic field lines simulation and winding partitioning **(A)** normal operating condition **(B)** inter-turn short circuit condition **(C)** inter-turn fault current and magnetic flux lines **(D)** Winding partition and measuring point location.

the differential leakage flux at the winding ends. The differential protection criterion for end regions is defined in Equation 5:

$$\Delta\Phi = \left|\Phi_{up} + K \cdot \Phi_{down}\right| > \Phi_{set} \tag{5}$$

The middle measurement point in the winding is used to assess the symmetry of the leakage magnetic field under normal operating conditions. For a symmetric winding, the middle leakage field value approaches zero. In cases where the winding structure is irregular, an inherent imbalance may exist, but the magnitude is much smaller than that under fault conditions. The imbalance at the middle measuring point is mainly determined by the physical structure and can thus be treated as a quasi-constant when compared to the

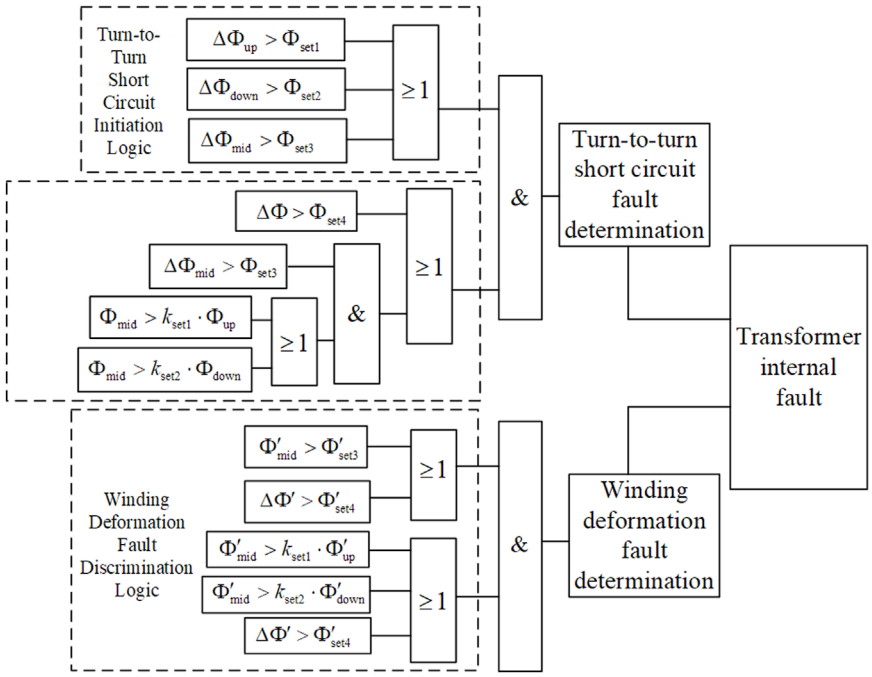


FIGURE 8
Logic diagram for early fault diagnosis, positioning, and protection decision of winding.

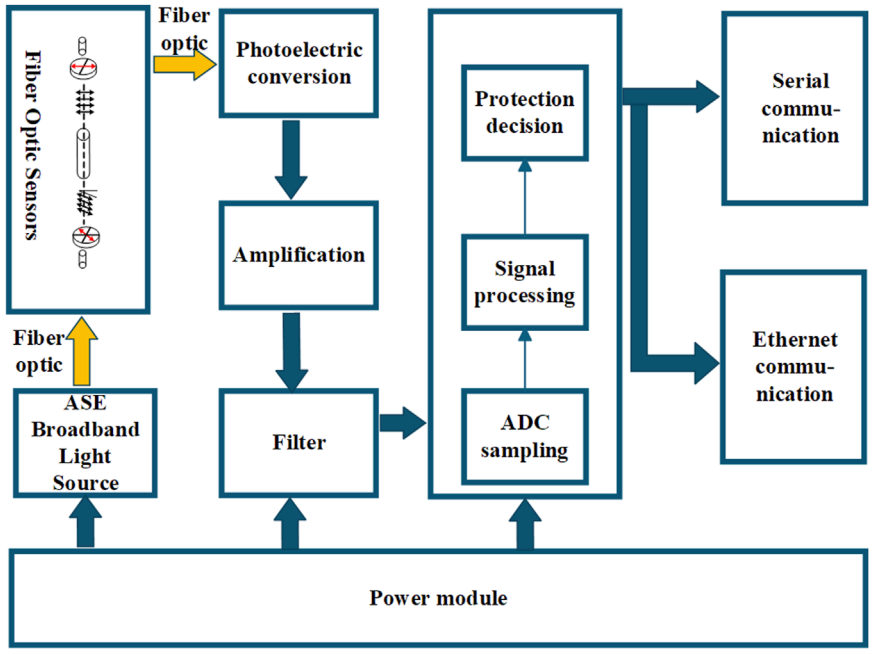


FIGURE 9
Hardware block diagram of protection device.

differential flux at the ends. The discrimination criterion for the middle point is given by Equation 6:

$$\Phi_{mid} > k_{set1} \cdot \Phi_{up} \quad (6)$$

Since mechanical deformation of the winding also alters the symmetry of the leakage magnetic field distribution, the same differential principle applies to detecting such deformation. Winding deformation is typically a cumulative abnormality.

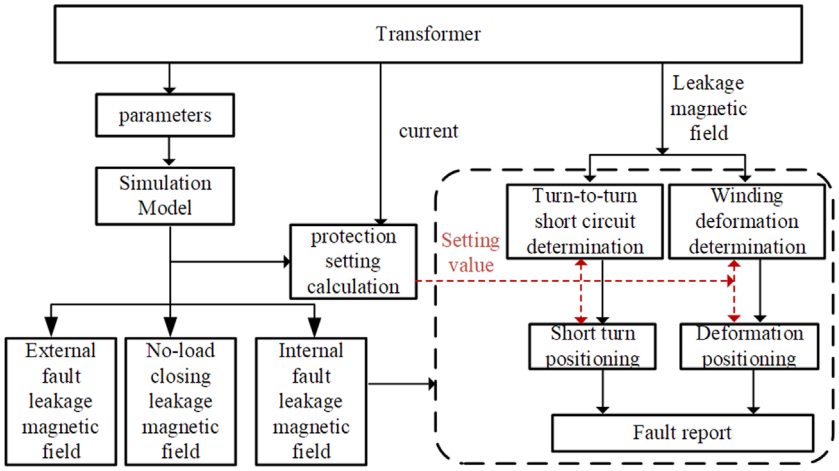


FIGURE 10
Principle of simulation and dynamic simulation joint experiment.

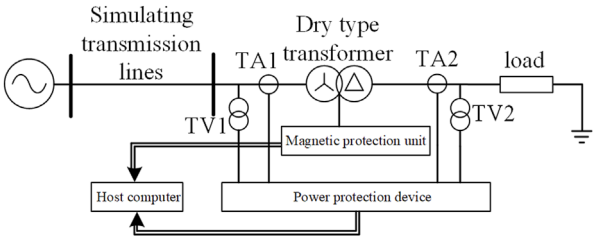


FIGURE 11
Early fault dynamic simulation experimental system for transformers.

Therefore, a fault initiation blocking condition is applied to ensure that this type of detection is performed only under steady-state operating conditions. By differentiating the activation threshold for inter-turn short-circuit faults and winding deformation, the detection sensitivity can be improved while reducing false alarms.

The complete protection logic is illustrated in Figure 8.

## 4.3 Setting of leakage magnetic field differential protection thresholds

The differential protection threshold for leakage magnetic field is determined based on the maximum magnetic flux imbalance that can occur at the transformer end under an external three-phase short-circuit fault. In this scenario, the maximum short-circuit current is assumed to be 20 times the rated current. Additionally, a horizontal positioning error of 0.05c is considered for the measuring points. By substituting the differential flux calculation formula into the analytical expression for the leakage magnetic field, the maximum leakage flux imbalance can be derived, as shown in Equation 7:

$$\begin{aligned}\Delta\Phi &= 20\left|\Phi(x,y_1+0.05c)+k\cdot\Phi(x,y_2)\right|+\varepsilon(x,y,r)\\ &= 20\sum_{m=1}^{\infty}\left\{\left|\begin{array}{l} L_1(x)\begin{bmatrix} D_1(y_1+0.05c)\\ +kD_1(y_2)\end{bmatrix}\left[e^{-m\frac{\pi}{\tau}h_W}-1\right]+\\ L_2(x)\begin{bmatrix} D_2(y_1+0.05c)\\ +kD_2(y_2)\end{bmatrix}\left[e^{0.75m\frac{\pi}{\tau}c}+1\right]\end{array}\right|\right\}\\ &\quad+\varepsilon(x,y,r)\end{aligned} \tag{7}$$

According to the two-dimensional structure of the transformer in this leakage magnetic field analytical model, the leakage magnetic flux value passing through the middle measurement area can be obtained by substituting the coordinates $(x,h_w/2+h_0)$ of the measuring point in the middle measurement area into the flux calculation formula of the analytical model. By comparing the leakage flux at the upper, middle, and lower measuring points, structural ratio coefficients $k_{set1}$ and $k_{set2}$ can be obtained to quantify the asymmetry of the winding geometry. Considering a reliability coefficient of 1.3, the final setting value for the differential protection threshold is given in Equation 8. The setting principles for coefficients $k$ and $k_{set2}$ follow the same methodology as used for $k_{set1}$.

$$\begin{aligned}k_{set1} &= 1.3\left|\frac{\Phi(x,h_w/2+h_0)}{\Phi(x,y_1)}\right|\\ &= 1.3\left|\frac{L_1(x)D_1\left(\frac{h_w}{2}+h_0\right)\left[e^{-m\frac{\pi}{\tau}h_w}-1\right]+L_2(x)D_2\left(\frac{h_w}{2}+h_0\right)\left[e^{0.75m\frac{\pi}{\tau}c}+1\right]}{L_1(x)D_1(y_1)\left[e^{-m\frac{\pi}{\tau}h_w}-1\right]+L_2(x)D_2(y_1)\left[e^{0.75m\frac{\pi}{\tau}c}+1\right]}\right|\end{aligned} \tag{8}$$

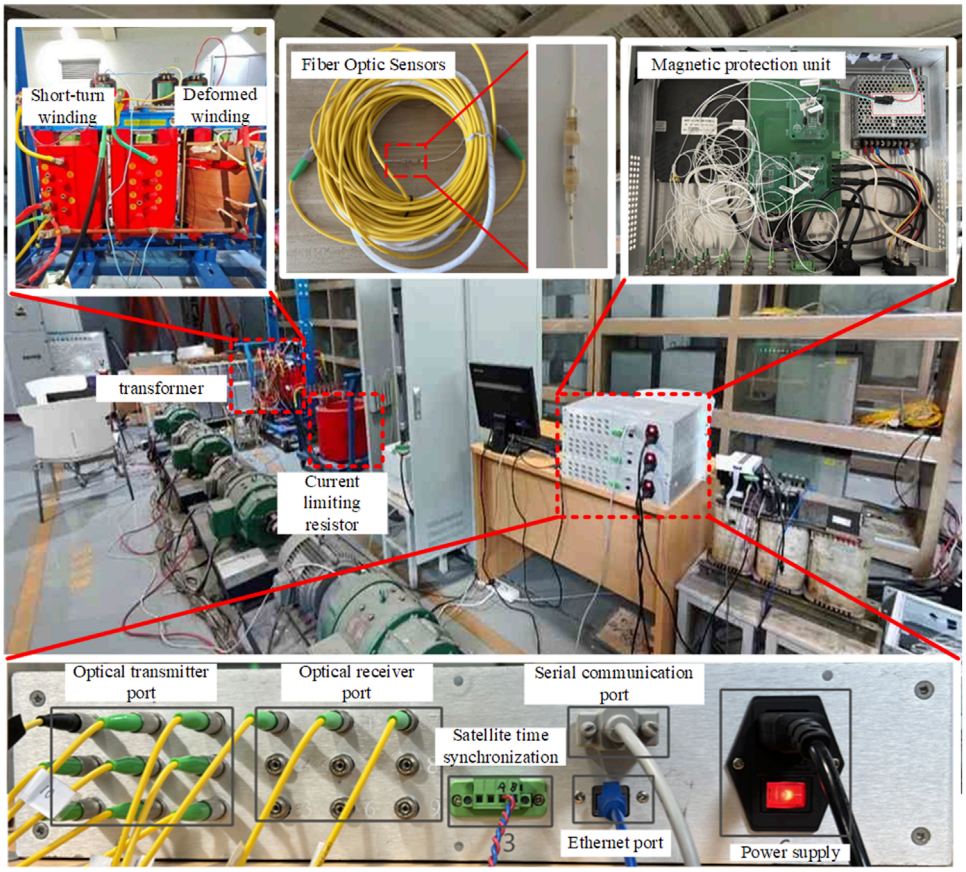


FIGURE 12
Dynamic simulation test of early fault protection device.

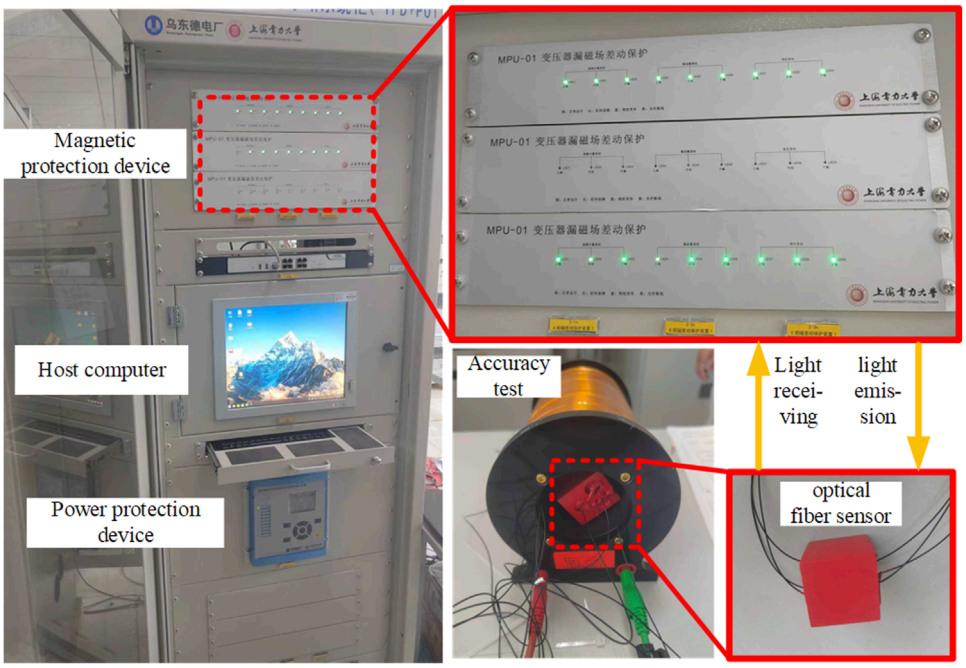


FIGURE 13
Accuracy testing of on-site application system and fiber optic sensor.

TABLE 3 Accuracy test results of fiber optic sensors.

| Channel number | Measurement data (mT) | | |
|---|---|---|---|
| | 0.1 A | 0.5 A | 0.9 A |
| 1 | 0.96 | 4.72 | 8.41 |
| 2 | 0.99 | 4.82 | 8.63 |
| 3 | 1.02 | 5.07 | 9.05 |
| 4 | 0.99 | 4.98 | 9.09 |
| 5 | 1.00 | 5.01 | 8.91 |
| 6 | 0.99 | 4.91 | 8.74 |
| 7 | 1.00 | 4.98 | 8.88 |
| 8 | 0.96 | 4.80 | 8.55 |
| 9 | 0.98 | 4.92 | 8.76 |
| Calibration Value | 0.99 | 4.92 | 8.83 |
| Maximum error% | 3.609 | 3.713 | 4.674 |

# 5 Dynamic simulation verification of leakage magnetic field differential protection device development

## 5.1 Development of the protection device

### 5.1.1 Fiber-optic sensor based on magneto-optical crystal

To measure the spatial distribution of the leakage magnetic field along the winding surface, multiple fiber optic sensors are required. However, magnetic field sensors based on interference principles are prohibitively expensive and difficult to apply in practice. In contrast, sensors based on the Faraday magneto-optical effect offer lower cost, sufficient accuracy, and are well-suited for large-scale deployment.

The core component of the fiber optic sensor is the magneto-optical crystal. In this study, Yttrium Iron Garnet (YIG) was selected (Wang et al., 2023). Operating in the near-infrared wavelength of 1,550 nm, YIG exhibits a Faraday rotation coefficient of 200°–300°/cm, significantly higher than that of traditional magneto-optic materials. This allows for effective modulation of the polarization state of light, making it highly sensitive to weak magnetic fields. Additionally, YIG has low optical absorption in the communication band, making it compatible with fiber-optic systems. The YIG crystal, optical components, and loops are encapsulated in a glass tube and connected via fiber tails to form the complete fiber optic sensor.

### 5.1.2 Hardware circuit of the magnetic quantity protection device

The hardware structure of the transformer early fault protection device, based on fiber optic leakage magnetic field sensors, is shown in Figure 9. The system includes a fiber optic sensor module, signal conditioning and conversion module, signal processing module, and power supply module. The signal processing module is built with a dual-core DSP operating at 200 MHz, equipped with an FPU and TMU, which are suitable for high-performance computation of leakage magnetic field signals and for executing protection algorithms.

The fiber optic sensors are installed at the upper, middle, and lower measuring points on the transformer winding. The parameters of the dynamic test system can be adjusted to match experimental requirements. A broadband ASE light source generates optical signals transmitted via fiber. When these signals pass through the magneto-optical crystal, the polarization direction is rotated due to the influence of the leakage magnetic field near the winding. After passing through the analyzer, the polarized light returns through the tail fiber to the protection device. The received signal is converted, filtered, and amplified before being processed by a DSP to perform Fast Fourier Transform (FFT). The protection device then identifies and localizes early-stage transformer faults based on the preset differential protection logic.

This device supports nine optical signal channels in total. Three optical channels are assigned to each of the upper, middle, and lower measuring points of the winding. This configuration supports either single-direction magnetic field measurement or full three-dimensional magnetic field analysis.

For minor inter-turn short-circuit faults, the device supports steady-state and transient magnetic differential protection, phase-difference-based protection, and fault localization. For winding deformation, the system offers steady-state magnetic field analysis and angular deviation-based deformation detection.

## 5.2 Dynamic simulation experimental study

While simulation models allow for quantitative verification of fault criteria, controlled initial conditions of excitation, and exploration of extreme cases such as minor or severe faults, physical dynamic simulations are limited to predefined fault types. Therefore, this study integrates both simulation and physical dynamic modeling for hybrid testing, as illustrated in Figure 10.

A simulation model was established based on the physical parameters of the transformer. Its results were verified for consistency with both analytical calculations and empirical measurements. The thresholds for protection were determined using the simulation outputs, and corresponding settings were fine-tuned. This hybrid approach allows for the verification of early fault detection schemes, especially under operating conditions that are difficult to reproduce in physical testing.

Since the fault signature used in this study is the leakage magnetic field, traditional digital dynamic simulation systems such as RTDS (Real-Time Digital Simulator), commonly used in relay protection development, are not suitable. A physical dynamic simulation system was therefore developed, capable of replicating early-stage transformer faults and mimicking grid operating conditions. This system is shown in Figure 11. The research team designed a modular transformer with configurable core and winding structures, including windings capable of simulating minor inter-turn short-circuits and deformation by adjusting physical dimensions. The short-circuit winding includes seven tapping points

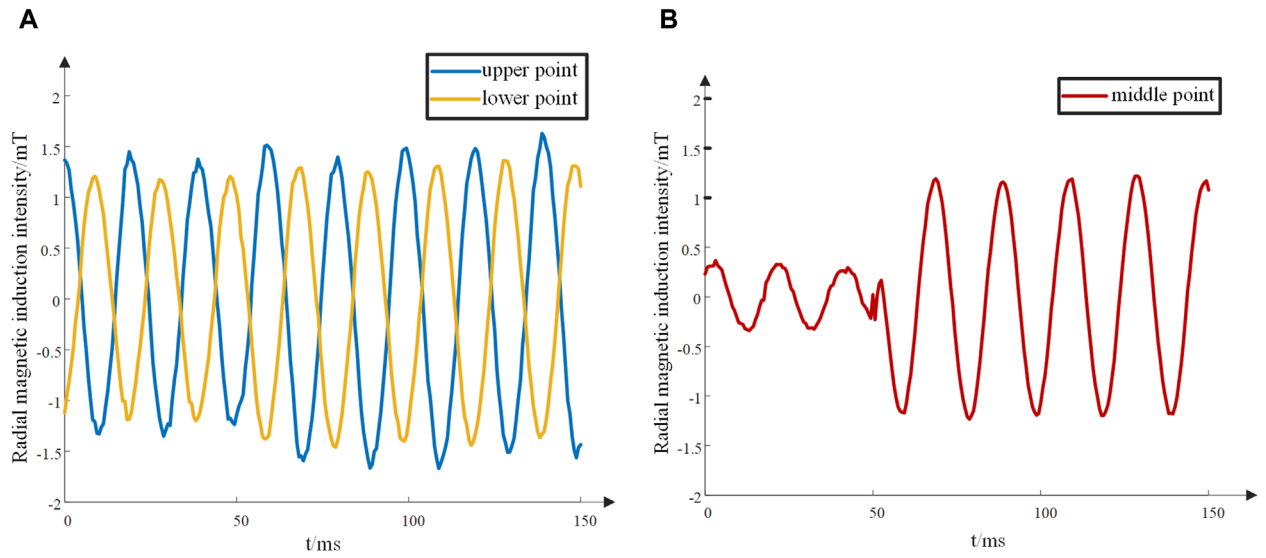


FIGURE 14
Waveform diagram of fault measurement points between two turns in the central region **(A)** upper and lower measurement values **(B)** middle measurement point value.

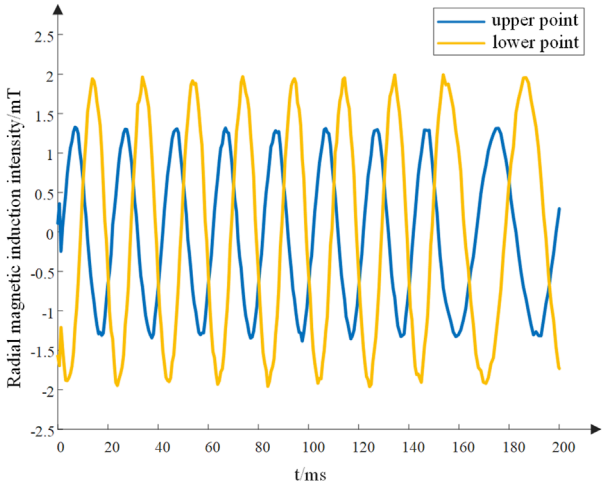


FIGURE 15
Waveform diagram of measurement points 1 and 2 when 10% winding compression deformation occurs at the upper end of the winding.

for external connection, where fixed resistors simulate minor inter-turn faults. Additionally, the windings can be connected to an arc discharge circuit to mimic arc-type faults. Fault locations can be set at upper, middle, or lower measuring points, and the system is capable of simulating various transformer operating conditions.

The developed physical dynamic simulation system and the associated protection device testing are shown in Figure 12. The leakage magnetic field-based early fault protection device was thoroughly tested, including evaluation of the fiber optic sensor alignment accuracy and the effectiveness of differential protection under early fault conditions. The final field-deployable system is illustrated in Figure 13 and is intended for use in a dry-type auxiliary transformer at a hydroelectric power plant.

## 5.3 Dynamic simulation verification

### 5.3.1 Static matching accuracy test for fiber optic channels

This test focuses on evaluating the consistency of all optical fiber measurement channels in the leakage magnetic field early fault protection device. The calibration procedure is illustrated in Figure 13. A relay protection tester is used to supply different AC currents to a solenoid, creating varying magnetic field strengths, against which the output of the optical fiber leakage magnetic field sensors is calibrated. The accuracy of leakage magnetic field measurement depends on the characteristics of the optical fibers. Different channel coefficients are configured to assess the matching degree across various fibers. If the matching degree is high, measurement accuracy becomes independent of the specific fiber used. The experiment tested 54 optical fiber measurement channels from 6 devices, with the overall average error not exceeding 5%.The test results of Device No. 1 are shown in Table 3.

### 5.3.2 Dynamic simulation test of transformer leakage magnetic field differential protection

To ensure safety during inter-turn short-circuit tests, a current-limiting resistor is inserted into the short-circuit loop, restricting the short-circuit current to approximately one-tenth of the metallic short-circuit level. When a 2-turn (1%) inter-turn fault occurs in the middle region of the winding, the waveforms of the three measuring points are shown in Figure 14.

The fault current generated by the inter-turn short circuit in the middle region creates a magnetic field that overlaps with the normal operating magnetic field. This superposition remains largely symmetric at the upper and lower measuring points, resulting in small values of the symmetric differential component. As seen in Figure 14A, the radial magnetic flux density at the upper and lower measuring points changes only slightly before and after the fault, maintaining the field symmetry. Despite limiting the maximum

TABLE 4 Summary table of tests.

| Fault type | Measurement data (mT) | | | Positioning | Time |
|---|---|---|---|---|---|
| | Sudden change in measurement point | Sudden variables at intermediate measurement points | Sudden changes in measurement points | | |
| Central region 2 short circuit between turns | 0.34 | 1.01 | 0.21 | central region | 30 m |
| Short circuit between the two turns in the lower area 2 | 0.11 | 0.52 | 1.34 | lower region | 30 m |
| No-load closing | / | / | / | Inaction | / |
| Airdrop in the middle inter turn short circuit | 0.41 | 1.12 | 0.27 | central region | 30 m |
| Upper 10% winding deformation | / | / | / | upper area | 30 m |

TABLE 5 Summary of action under out of area fault conditions verified by finite element simulation.

| Fault type | Measurement data (mT) | | | Positioning | Time |
|---|---|---|---|---|---|
| | Measurement point 1: Sudden variable | Measurement point 3: Sudden variable | Measurement point 2: Sudden variable | | |
| Fault outside the area | / | / | / | Inaction | / |
| Out of zone fault, lower area 1 has a short circuit between turns | 3.24 | 5.38 | 27.86 | lower region | 30 m |

TABLE 6 Comparison of leakage magnetic field differential protection and induced-voltage-based protection.

| Protection scheme | Fault condition | Fault characteristic quantity | | | Action status |
|---|---|---|---|---|---|
| | | $\Delta B_{up}$/mT | $\Delta B_{mid}$/mT | $\Delta B_{down}$/mT | |
| Leakage flux differential protection | Phase A upper 0.5% | 1.63 | 14.2 | 2.61 | Operate |
| | Phase A middle 0.5% | 10.75 | 1.83 | 1.01 | Operate |
| Crt_SUM / mV | | | | | |
| Leakage flux induced voltage protection | Phase A upper 1.13% | 245.1 | | | Operate |
| | Phase A middle 1.13% | 39.3 | | | No operation |

short-circuit current for winding protection purposes, Figure 14B shows that the magnetic flux density at the middle measuring point increases significantly after the fault, satisfying the inter-turn fault discrimination criteria and accurately indicating that the fault occurred in the central part of the winding.

Winding deformation tests require that deformation be applied prior to energization, as such faults typically exhibit long-term and stable behavior. A 10% compression deformation is applied to the upper end of the winding. The steady-state waveforms at the upper and lower measuring points are shown in Figure 15.

Under normal operating conditions, the radial magnetic flux density at the upper and lower measuring points is symmetric. After compensating for asymmetry using a balance coefficient, the differential flux value remains near zero. Clearly, after the winding

deformation fault occurs, the measured value at the upper point decreases significantly, meeting the fault detection criteria and indicating that the deformation is located at the upper part of the winding.

A summary of the dynamic simulation test results for various fault conditions is presented in Table 4.

### 5.3.3 Finite element model validation

Due to experimental limitations, finite element simulation is used to validate the system's response under external fault conditions. The results are summarized in Table 5.

## 5.4 Analysis of experimental results

Based on the results of both dynamic simulation and finite element analysis, it is evident that the steady-state leakage magnetic field differential protection scheme is capable of responding to a one-turn short circuit within 30 milliseconds. It is immune to the effects of magnetizing inrush current and can accurately locate the fault point. The transient differential protection scheme based on magnetic field variation also effectively detects minor inter-turn faults involving a single turn. It responds within 25 milliseconds and remains unaffected by inrush current. For winding deformation detection, the steady-state magnetic field–based method effectively identifies a 10% compression deformation at both the upper and lower ends of the winding and accurately locates the deformation. Moreover, each measurement point is equipped with three redundant sensors, ensuring that the protection functionality remains unaffected even if any two of the three channels are disconnected or malfunction.

## 5.5 Verification of the superiority of leakage magnetic field differential protection

To highlight the superiority of the proposed scheme, we compare our differential protection method with Haghjoo et al. (2018). The method in this also identifies transformer faults based on magnetic-field symmetry, but it derives the leakage magnetic field indirectly from the induced voltage of search coils, whereas the present work measures the leakage magnetic field directly using fiber-optic sensors. A detailed comparison is provided in Table 6. Although the fiber-optic approach does not show a pronounced advantage in raw measurement accuracy or response time for transformer fault identification, it provides strong immunity to electromagnetic interference, eliminates high-voltage insulation risks, and allows flexible sensor deployment at different winding locations to satisfy symmetry-based measurement requirements—thereby offering a clear advantage in fault localization. In the referenced method, a fixed threshold of 150 mV leads to unreliable operation when an inter-turn short circuit occurs in the middle of the winding, necessitating further analysis of the remaining waveforms composing Ctr_SUM, or even using voltage waveforms from five sensors per phase, to reach a correct decision. By contrast, our method avoids interference and high-voltage insulation issues inherent to magnetic-field measurement, providing essential practical support for achieving high-precision fault localization and for subsequent extensions to multidimensional measurement applications.

# 6 Conclusion

This study begins by analyzing the practical limitations of conventional transformer online monitoring and traditional differential protection systems. A novel protection principle is proposed, which leverages the variations in leakage magnetic field distribution caused by winding faults to sensitively detect early-stage transformer failures. A prototype device was developed, and a physical dynamic simulation system was constructed to experimentally validate this principle under both static and dynamic conditions. The main conclusions are as follows:

A finite element simulation model was established based on the actual structure of a physical transformer, enabling the analysis of winding leakage magnetic field characteristics under various operating conditions.

The spatial symmetry of the leakage magnetic field exhibits clear and predictable patterns. These features were employed to formulate fault identification and localization criteria, and the corresponding protection settings were established accordingly.

A prototype protection device was developed. For each phase winding, three magneto-optical sensors were installed at the upper, middle, and lower positions to acquire leakage magnetic field intensity data. Optical signals are transmitted via optical fibers to the magnetic differential protection device, where photoelectric conversion and analog-to-digital conversion are performed before the data are processed by an embedded system. Upon fault occurrence, the system completes fault identification and localization within 30 milliseconds, issues alarms and trip signals, and generates a detailed fault report.

# Data availability statement

The original contributions presented in the study are included in the article/supplementary material, further inquiries can be directed to the corresponding author.

# Author contributions

JW: Writing – original draft, Writing – review and editing. ZT: Conceptualization, Writing – review and editing. KZ: Writing – review and editing, Investigation. YL: Data curation, Writing – review and editing. XD: Writing – review and editing, Project administration. HT: Data curation, Writing – review and editing.

# Funding

The author(s) declare that financial support was received for the research and/or publication of this article. Funded by China Yangtze Power Co. Ltd. (Funding Project No. Z522302029). The funder was not involved in the study design, data collection and analysis, decision to publish, or preparation of the manuscript.

## Acknowledgments

The authors gratefully acknowledge the support of China Yangtze Power Co., Ltd. (Funding Project No. Z522302029) and Shanghai University of Electric Power for the development of the present study.

## Conflict of interest

Authors JW, ZT, KZ, and YL were employed by China Yangtze Power Company.

The remaining authors declare that the research was conducted in the absence of any commercial or financial relationships that could be construed as a potential conflict of interest.

## Generative AI statement

The author(s) declare that Generative AI was used in the creation of this manuscript. The authors confirm the use of generative AI technology solely for language refinement purposes during manuscript preparation. AI-assisted tools were employed exclusively to enhance grammar, syntax, and fluency of translated content. All scientific content, data interpretation, and conclusions remain entirely human-generated and validated. The authors take full responsibility for the work.

Any alternative text (alt text) provided alongside figures in this article has been generated by Frontiers with the support of artificial intelligence and reasonable efforts have been made to ensure accuracy, including review by the authors wherever possible. If you identify any issues, please contact us.

## Publisher's note



## References

Abi-Samra, N., Arteaga, J., Darovny, B., Foata, M., Herz, J., Lee, T., et al. (2009). Power transformer tank rupture and mitigation—A summary of current state of practice and knowledge by the task force of IEEE power transformer subcommittee. *IEEE Trans. Power Deliv.* 24, 1959–1967. doi:10.1109/TPWRD.2009.2028817

Brodeur, S., and Dastous, J.-B. (2020). Design and testing of an arc resistant power transformer tank. *IEEE Trans. Power Deliv.* 35, 699–706. doi:10.1109/TPWRD.2019.2922505

Deng, X., Zhu, H., Yang, M., Wu, W., and Liu, S. (2022). Research on early fault protection method of transformer winding based on multi-state model. *Proc. CSEE* 42, 6704–6715. doi:10.13334/j.0258-8013.pcsee.211653

Deng, X., Yan, K., Zhu, H., Zhu, H., Zhang, Z., and Liu, S. (2023a). Transformer winding early fault protection based on circuit-magnetic leakage field multi-state analytical model. *Power Syst. Technol.* 47, 3808–3821. doi:10.13335/j.1000-3673.pst.2022.2015

Deng, X., Zhang, Z., Zhu, H., and Yan, K. (2023b). Early fault diagnosis of transformer winding based on leakage magnetic field and DSAN learning method. *Front. Energy Res.* 10, 1058378. doi:10.3389/fenrg.2022.1058378

Deng, X., Zhu, H., Yan, K., Zhang, Z., and Liu, S. (2024). Magnetic balance protection of transformers based on optical fiber leakage magnetic field measurement. *Trans. China Electrote-chnical Soc.* 39, 628–642. doi:10.19595/j.cnki.1000-6753.tces.221959

Gomathi, R., Arunkumar, R., Preethi, S. T., Arunprakash, P. V., and Karkuzhali, G. (2023). "A novel technique for differential protection for resistance grounded three phase transformer using wavelet packet transformer," in 2023 International Conference on Sustainable Communication Networks and Application (ICSCNA), Theni, India (IEEE), 714–719.

Haghjoo, F., Mostafaei, M., and Mohammadi, H. (2018). A new leakage flux-based technique for turn-to-turn fault protection and faulty region identification in transformers. *IEEE Trans. Power Deliv.* 33, 671–679. doi:10.1109/tpwrd.2017.2688419

Hou, Y., Zhou, Q., Ouyang, X., Chen, W., and Dong, R. (2024). Reflective magnetic field sensor based on magneto-optical crystal and fiber bragg grating. *Acta Opt. Sin.* 44, 280–290. doi:10.3788/AOS240579

Huang, M., Zheng, W., Ji, T., Ji, M., Pu, T., and Qi, B. (2024). Optical sensor with wide range and high sensitivity for internal magnetic field detection of transformer. *CSEE J. Power Energy Syst.* 10, 2230–2244. doi:10.17775/CSEEJPES.2022.07270

Ji, M., Qi, B., Zheng, W., Huang, M., Li, C., and Wang, J. (2024). Coding diagnosis method based on leakage distribution law under typical winding defects of transformers. *Power Syst. Technol.* 48, 2133–2142. doi:10.13335/j.1000-3673.pst.2023.1694

Jiang, J., Wu, Z., Sheng, J., Zhang, J., Song, M., Ryu, K., et al. (2021). A new approach to measure magnetic field of high-temperature superconducting coil based on magneto-optical faraday effect. *IEEE Trans. Appl. Supercond.* 31, 1–5. doi:10.1109/TASC.2020.3032134

Li, J., Zhao, Y., Wen, T., Fan, X., Chen, W., Zhang, Q., et al. (2021). "An optical fiber magnetic field sensor based on faraday effect for transformer leakage magnetic field measurement," in 2021 IEEE Electrical Insulation Conference (EIC), Denver, CO, USA (IEEE), 137–140.

Liu, J., Li, Z., and Zhou, Y. (2024a). Transformer windin-gs based on leakage field and ICOA-ResNet early fault diagnosis. *Power Syst. Prot. Control* 52, 99–110. doi:10.19783/j.cnki.pspc.231278

Liu, J., Dong, Q., Tian, S., Liu, M., Mei, Z., and Zhou, H. (2024b). Early fault diagnosis of transformer winding based on ReliefF-mRMR leakage magnetic field feature optimization and improved LSSVM. Available online at: https://kns.cnki.net/KCMS/detail/detail.aspx?dbcode=CAPJ&dbname=CAPJLAST&filename=DCYQ20240508005 (Accessed February 27, 2025).

Mirowski, P., and LeCun, Y. (2012). Statistical machine learning and dissolved gas analysis: a review. *IEEE Trans. Power Deliv.* 27, 1791–1799. doi:10.1109/TPWRD.2012.2197868

Wang, S., Zhang, H., Wang, S., Li, H., and Yuan, D. (2016). Cumulative deformation analysis for transformer winding under short-circuit fault using magnetic–structural coupling model. *IEEE Trans. Appl. Supercond.* 26, 0–5. doi:10.1109/TASC.2016.2584984

Wang, P., Zhu, M., Pang, F., Wei, H., Zhang, L., Shang, Y., et al. (2023). Cylindrical vector beams for alternating magnetic field sensing based on YIG crystal. *IEEE Phot. Technol. Lett.* 35, 1031–1034. doi:10.1109/LPT.2023.3297980

Xian, R., Wang, L., Zhang, B., Li, J., Xian, R., and Li, J. (2024). Identification method of interturn short circuit fault for distribution transformer based on power loss variation. *IEEE Trans. Ind. Inf.* 20, 2444–2454. doi:10.1109/TII.2023.3292972

Yamagashira, M., Wakabayashi, D., and Enokizono, M. (2014). Vector magnetic properties and 2-D magnetostriction of various electrical steel sheets under rotating flux condition. *IEEE Trans. Magn.* 50, 1–4. doi:10.1109/TMAG.2013.2290836

Yan, C., Liu, H., Yang, H., Yang, X., Zhang, P., and Zhang, B. (2024). Toward a novel characterization of transformer interturn faults based on arc-induced transients in winding magnetomotive force. *IEEE Trans. Magn.* 60, 1–6. doi:10.1109/TMAG.2024.3429367

Zhang, H., Li, F., Guo, H., Yang, Z., and Yu, N. (2019). Current measurement with 3-D coreless TMR sensor array for inclined conductor. *IEEE Sens. J.* 19, 6684–6690. doi:10.1109/JSEN.2019.2914939

Zhang, B., Xian, R., Yu, Y., Xie, T., Gao, H., and Chen, L. (2021). Analysis of physical characteristics of power transformer windings under inter-turn short circuit fault. *High. Volt. Eng.* 47, 2177–2185. doi:10.13336/j.1003-6520.hve.20201178

Zheng, Y., Gong, X., Pan, S., Sun, J., and Deng, J. (2022). Analysis on leakage flux characteristics of turn-to-turn short-circuit fault for power transformer. *Automation Electr. Power Syst.* 46, 121–127.

Zhou, Y., and Wang, X. (2017). The on-line monitoring method of transformer winding deformation based on magnetic field measurement. *Electr. Meas. and Instrum.* 54, 58–63.

## Nomenclature

| | |
|---|---|
| $A_{zI}$, $A_{zII}$ and $A_{zIII}$ | Vector magnetic potential in region I, II and III |
| $B_{xI}$, $B_{xII}$ and $B_{xIII}$ | Radial magnetic induction intensity in region I, II and III |
| $D_1$ and $D_2$ | The coefficients of the regular component and the superposition component of the magnetic field analytical formula that are related to the axial position y respectively |
| $h_0$ | Distance between the low-voltage winding and the upper/lower yoke |
| $h_{1-4}$ | Height of the irregular windings in the high-voltage winding required for insulation and testing purposes |
| $J_z$ | Current density |
| $J_{1A}$ and $J_{2A}$ | Current density in A phase high-voltage winding and low-voltage winding respectively |
| $J_{1A-in}$ and $J_{1A-out}$ | The current density of the A-phase high-voltage inner and outer winding of the Regular Component respectively |
| $K$ | Photoelectric conversion coefficient |
| $K_{set}$ | Adjustment factor for magnetic flux difference |
| $k_{set1}$ | The structural ratio coefficient of the middle measuring point relative to the upper measuring point |
| $k_{set2}$ | The structural ratio coefficient of the middle measuring point relative to the lower measuring point |
| $L_1$ and $L_2$ | The coefficients of the regular component and the superposition component of the magnetic field analytical formula that are related to the radial position y respectively |
| $L_i$ | Input light intensity |
| $V$ | Verdet constant of the magneto-optic material |
| $w_0$, $w_2$ and $w_5$ | The distance between the iron core and the low-voltage winding, the low-voltage winding and the high-voltage winding, the high-voltage winding and the neutral line respectively |
| $w_1$, $w_3$ and $w_4$ | Thickness of the low-voltage winding, the inner layer of the high-voltage winding and the outer layer of the high-voltage winding |
| $\alpha$ | Light absorption coefficient of the magneto-optical medium |
| $\beta$ | Angle between the transmission axis of the polarizer and the polarization plane of the incident polarized light, generally set to 45° |
| $\varepsilon$ | Errors related to environmental factors |
| $\theta$ | Faraday rotation angle |
| $\mu_0$ | Magnetic permeability of vacuum |
| $\mu_{Fe}$ | Magnetic permeability of the iron core |
| $\tau$ | Distance from the iron core to the neutral line |
| $\Delta\Phi$ | The imbalance of the radial leakage magnetic flux at the winding ends under turn-to-turn short circuit fault |
| $\Delta\Phi'$ | The imbalance of the radial leakage magnetic flux at the winding ends under winding deformation |
| $\Phi_{up}$, $\Phi_{mid}$ and $\Phi_{down}$ | The measured magnetic flux values of the leakage magnetic field at the upper, middle, and lower measuring points under turn-to-turn short circuit fault respectively |
| $\Phi'_{up}$, $\Phi'_{mid}$ and $\Phi'_{down}$ | The measured magnetic flux values of the leakage magnetic field at the upper, middle, and lower measuring points under winding deformation respectively. |